

Fjords in viscous fingering: selection of width and opening angle

Leif Ristroph¹, Matthew Thrasher^{1,*} Mark B. Mineev-Weinstein², and Harry L. Swinney¹

¹Center for Nonlinear Dynamics and Department of Physics, University of Texas at Austin, Austin, Texas 78712 USA

²Applied Physics Division, MS-P365, Los Alamos National Laboratory, Los Alamos, New Mexico 87545 USA

(Dated: December 2, 2024)

Our experiments on viscous fingering of air into oil contained between closely spaced plates reveal two selection rules for the fjords of oil that separate fingers of air. (Fjords are the building blocks of solutions of the zero surface tension Laplacian growth equation.) Experiments in rectangular and circular geometries yield fjords with base widths $\frac{1}{2}\lambda_c$, where λ_c is the most unstable wavelength from a linear stability analysis. Further, fjords open at an angle of $8.0 \pm 1.0^\circ$. These selection rules hold for a wide range of pumping rates and fjord lengths, widths, and directions.

PACS numbers: 47.54.+r, 47.20.Ma, 68.35.Ja, 47.20.-k

Similar growth patterns have been found for viscous fingering, bacterial growth, flame propagation, dielectric breakdown, electrodeposition, solidification, metal corrosion, and diffusion limited aggregation (DLA) [1]. Analysis of these interfacial patterns is daunting because of the broad range of length scales, as illustrated by our experiments on fingering of air in thin oil layers (Fig. 1). The figure illustrates the increasing ramification of the interface that occurs with increasing forcing strength, characterized by the capillary number,

$$Ca = \frac{\mu V}{\sigma}, \quad (1)$$

where μ is the viscosity of the oil, V is the local interfacial velocity, and σ is the surface tension of the air-oil interface.

Most theoretical work on viscous fingering has concentrated on fingers rather than fjords, but fjords have been considered as building blocks of a theory of Laplacian growth in an analysis of a two-dimensional inviscid fluid penetrating a viscous fluid (with zero interfacial tension) [2]. These exact solutions for the interface are free of finite time singularities and are linear combinations of logarithmic terms, each term representing a single straight fjord with parallel walls. While these analytic solutions have helped in the understanding of the growth of complex growth patterns, experiments indicate fjords can have curved trajectories and nearly always have a nonzero opening angle [see Fig. 1] [3].

Most experiments have also concentrated on fingers, but a few experiments have examined fjords [3]. For the circular sector (“wedge”) geometry, Thomé et al. measured the angular gap between a wall and a divergent finger to be approximately 5° for divergent sector angles between 20° and 50° [4]. They introduced a method of sector decomposition in which ramified patterns were reduced to growth within wedges of varying angle whose “virtual walls” were fjord centerlines. Assuming that a fjord centerline acts like a wall, we conclude that the fjord

opening angle should be about 10° , twice the angle measured by Thomé et al. [4]. Since fjords are generally not symmetric about the centerline, the fjord opening angle is not expected to be exactly twice the angle measured by Thomé. Later theoretical work obtained the finger’s shape analytically [5, 6] and estimated a gap angle that would correspond to a fjord opening angle of 11.7° [6]. Other work has suggested that the width of a fjord relative to the width of the splitting finger has values between $\frac{1}{8}$ and $\frac{1}{3}$ [3, 4, 7, 8]. Also, Lajeunesse and Couder proposed a method for determining fjord centerlines and predicted the probability distribution of fjord lengths in the rectangular and wedge geometries [3].

Despite much effort, selection laws are lacking for ramified fingers in both rectangular [Fig. 1(a) and (b)] and circular geometries [Fig. 1(c) and (d)]. We find that fjords in both rectangular and circular geometries have a well-defined base width that is completely determined by the characteristics of the interface just prior to the fjord’s birth (when a tip splits). Further, we find that fjords open at an almost invariant angle. The selection rules for the fjord width and opening angle hold for a wide variation in the ramification of the patterns.

Experimental apparatus.— Interfacial patterns were grown in both rectangular and circular Hele-Shaw cells (closely spaced glass plates) filled with oil. Air was forced into the oil, creating an unstable interface (Fig. 1). In the rectangular geometry, two pieces of glass (each 1.91 cm thick), separated by a gap of 0.0508 cm, bounded a cell 25.4 cm wide by 254 cm long [9]. The maximum variation in gap thickness at the center of the cell (due to the imposed pressure gradient) was less than 3% even at the highest pump rate [9]. The cell was filled with silicone oil (viscosity $\mu = 50.6$ mPa·s and surface tension $\sigma = 20.5$ mN/m at laboratory temperature, 24°C); the oil wets the glass completely. A uniform flow rate was achieved using a precision syringe pump to withdraw oil from a reservoir at one end of the channel; an air reservoir at atmospheric pressure was attached to the other end. The channel was illuminated from below, and for each run 11 images (each 1300×1030 pixels, 0.21 mm/pixel) were obtained using a camera and rotating mirror. Concatenation of these images gave full interfaces, as in Fig. 1

*Electronic address: thrasher@chaos.utexas.edu

(a) and (b). Alternatively, good time resolution (up to 12 frames/s) was achieved with the camera focused on a fixed 22 cm long section of the channel, as shown in Fig. 2(a).

In the radial geometry, air was forced into an oil-filled gap through a hole in the center of the bottom glass plate. Each optically polished glass plate had diameter 28.8 cm and thickness 6.0 cm. The two plates were separated by a gap thickness of 0.0127 cm (uniform to 1%) [10, 11]. The gap and an annular reservoir were filled with silicone oil (viscosity $\mu = 345$ mPa·s and surface tension $\sigma = 20.9$ mN/m at 24 °C). Interfacial patterns were grown either by maintaining a constant pressure difference between the oil reservoir and air, or by using a syringe pump to remove oil from the buffer at a specified rate. Images of resolution 0.32 mm/pixel were acquired at up to 12 frames per second.

Fjord characteristics.—From the images we determined tip velocity V , tip curvature κ , fjord width W , and fjord opening angle ψ as a function of time (Fig. 2). The most unstable (critical) wavelength of a curved interface between a less viscous fluid forced into a more viscous fluid is given by [12, 13],

$$\lambda_c = \frac{\pi}{\sqrt{\frac{Ca}{b^2} + \frac{\kappa^2}{12}}} \approx \frac{\pi b}{\sqrt{Ca}} = \pi b \sqrt{\frac{\sigma}{\mu V}}, \quad (2)$$

where b is the cell gap thickness, and κ is the interface curvature (not including the curvature in the small gap dimension) at the point where it becomes unstable. For all interfaces that we examined, the curvature term in Eq. (2) was about two orders of magnitude smaller than the term involving the capillary number Ca ; hence we made the flat interface ($\kappa = 0$) approximation in computing λ_c . Chen performed experiments to test the instability wavelength as a function of Ca [14].

When a tip became unstable, the finger flattened and a fjord was born. A normal projection algorithm was used to track the fjord base back in time to earlier interfaces [solid, nearly straight line on the left in Fig. 2(a)]. (The base point for an earlier interface was located by projecting a ray normally from the later interface until it intersected the earlier one.) The time evolution of the local curvature κ then revealed the birth of the fjord, where $\kappa = 0$ [cf. Fig. 2(b)]. The velocity V_0 at this point [cf. Fig. 2(c)] was used in Eq. (2) to obtain a prediction for the selected fjord base width W_0 .

Once a fjord developed, we determined its width W along the arc length ℓ of its centerline, as illustrated in Fig. 2(d). The fjord centerline is found as follows: beginning with a point on the side of the fjord, the closest point on the opposite side is chosen, such that the interior angle between the two local tangents and the line connecting the two points is the same. The midpoint of the connecting line is on the fjord centerline. The rest of the centerline is found by repeating this procedure on the other points of the fjord. An arc length of $\ell = 0$ corresponds to the fjord base point [see Fig. 2(b)], where the

curvature is both a minimum along the interface and a minimum along the trajectory found by the normal projection algorithm. All arc lengths are measured from this point. As surface tension relaxes the interface, the fjord's base moves forward. The distance the base moves after $t = 0$ was corrected by adding the same distance to the arc length [see Fig. 2(d)].

Curves $W(\ell)$ obtained for different fjords were found to exhibit the same structure: $W(\ell)$ grew quickly at first due to the rounded nature of the fjord base, but soon it increased linearly. The selected fjord base width W_0 was measured as follows: the local tangent of $W(\ell)$ was linearly extrapolated back to $\ell = 0$ for all points on the centerline, a histogram of projected base widths was collected, and the histogram's peak gave W_0 .

The linear increase in $W(\ell)$ also suggests an almost constant opening angle: $\psi = \arctan(\frac{dW}{d\ell})$. We found that $\psi(\ell)$ has the same qualitative evolution for all fjords. By definition, the fjord begins with an opening angle of 180°, followed by a surface tension-induced dip for small ℓ , followed by a peak, and finally a rapid increase at the fjord's end. The selected opening angle ψ_0 was obtained from the peak of the histogram of ψ values generated from plots of $\psi(\ell)$ like Fig. 2(e). The angle selected was remarkably robust, always about 8°, even for fjords with many nearby fjords, though $\psi(\ell)$ for large ℓ was more strongly affected by neighboring fjords.

Fjord base width.—We predict that the base width of a fjord is determined at the birth of the instability of the moving interface, as illustrated by the inset of Fig. 3. The critical wavelength λ_c given by a linear stability analysis of the initial flat front, Eq. (2), determines the distance between adjacent fingers when they are born, and the base width of the fjord that develops between the two emergent fingers is $W_0 = \frac{1}{2}\lambda_c$. A comparison between the predicted widths and measurements requires a value for the velocity V in the capillary number Ca . We assumed $V = V_0$, the tip velocity at the onset of instability, where $\kappa = 0$ [see Fig. 2(b) and (c)].

Measurements of the selected fjord base width W_0 in both the circular and rectangular geometries agree well with the predicted width, as Fig. 3 illustrates. The fjord widths vary by an order of magnitude. The pump rates used were 0.17-2.00 cm³/s in the rectangular cell and 0.00083-0.033 cm³/s in the circular cell. Also, measurements in the circular cell were made with constant pressure differences of 0.10 and 0.25 atm. Global forcing strength does not completely determine the width of each fjord; instead, the local forcing strength at a fjord's birth determines its width. The local forcing strength is affected by nearby fjords, walls, and details of the interface. Therefore, a specific global pumping rate can yield a collection of fjords with different properties.

Fjord opening angle.—The selected opening angle ψ_0 measured in the rectangular geometry is shown in Fig. 4(a) as a function of the appropriate forcing parameter for this geometry, the modified capillary number, $1/B = 12 Ca (w/b)^2$, which combines the aspect ratio

w/b (where w is the channel width) and the capillary number Ca [9, 15]. This modified capillary number was computed using the average velocity of the furthest finger tip. Isolated fjords occur in the regime just beyond the onset of tip splitting, which occurs for $1/B \approx 4000$ [15]. The isolated fjords have a selected opening angle $\psi_0 = 6.3 \pm 0.4^\circ$. For $1/B > 25000$, the pattern develops a high density of fjords. Within the experimental uncertainty, all fjords grown in this regime have the same selected opening angle, $\psi_0 = 7.9 \pm 0.8^\circ$.

The results for the distribution of opening angles in the circular cell are indistinguishable from those for ramified patterns in the rectangular cell: the distribution function has the same form with the same mean, 8° , and same standard deviation, 1° [Fig. 4(b)]. This result is presumably related to the selection problem studied in a sector of a circle, where, as mentioned previously, an opening angle of about 10° can be deduced from past experiments in the sector geometry [4].

We believe that the near constancy of the opening angle is fundamental to scale invariance and fractal dimension. This result is consistent both with phenomenological efforts to relate the multifractal dimensions of a fully developed fingering structure with the fjords' opening angle [16] and with a recent observation [11] of an invariant unscreened angle distribution in a fractal grown in a radial geometry. While intriguing, the connection between these invariant geometrical characteristics remains obscure.

Conclusions.—We have presented two selection rules for the geometric form of fjords in rectangular and circular geometries. The selected base width of fjords has been shown to be well-described by $W_0 = \frac{1}{2}\lambda_c$, where λ_c is the local critical wavelength. This rule holds for a wide range of fjord widths, lengths, and degrees of bending, and for a wide range of angles of fjord directions with respect to the rectangular cell axis or with respect to radial lines in the circular cell. The fjord width selection rule provides insight into the most apparent difference in viscous fingering patterns: highly forced patterns are composed of thinner fjords. With increasing forcing, the fundamental length scale decreases while the opening angle is nearly constant.

We also found that fjords in both rectangular and circular geometries open at a nearly constant angle of 8° with a 1° standard deviation. This angle depends at most weakly on the local interfacial characteristics. The same angle is selected for different pumping rates and fjord widths, lengths, and directions. We have no explanation for this result.

We thank W.D. McCormick, Mitchell Moore, Olivier Praud, and Jack Swift for helpful discussions. This work was supported by the Office of Naval Research Grant N00014-04-1-0282, the Office of Naval Research Quantum Optics Initiative Grant N00014-03-1-0639, and by Los Alamos National Laboratory LDRD Grant “Unstable fluid/fluid interfaces.”

[1] Y. Couder, *Perspectives in Fluid Dynamics*, edited by G. K. Batchelor, H. K. Moffat, and M. G. Worster (Cambridge University Press, Cambridge, 2000), pp. 53–104.
[2] M. B. Mineev-Weinstein and S. P. Dawson, Phys. Rev. E **50**, R24 (1994).
[3] E. Lajeunesse and Y. Couder, J. of Fluid Mech. **419**, 125 (2000).
[4] H. Thomé, M. Rabaud, V. Hakim, and Y. Couder, Phys. Fluids A **1**, 224 (1989).
[5] M. BenAmar, Phys. Rev. A **43**, R5724 (1991).
[6] Y. Tu, Phys. Rev. A **44**, 1203 (1991).
[7] L. Paterson, J. Fluid Mech. **113**, 513 (1981).
[8] A. Pereira and J. Elezgaray, Phys. Rev. E **69**, 026301 (2004).
[9] M. G. Moore, A. Juel, J. M. Burgess, W. D. McCormick, and H. L. Swinney, Phys. Rev. E **65**, 030601(R) (2002).
[10] E. Sharon, M. G. Moore, W. D. McCormick, and H. L. Swinney, Phys. Rev. Lett. **91**, 205504 (2003).
[11] O. Praud and H. L. Swinney, Phys. Rev. E **72**, 011406 (2005).
[12] R. L. Chooke, P. van Meurs, and C. van der Pol, Trans. AIME **216**, 188 (1959).
[13] J. Bataille, Revue Inst. Pétrole **23**, 1349 (1968).
[14] J.-D. Chen, J. Fluid Mech. **201**, 223 (1989).
[15] C. W. Park and G. M. Homsy, Phys. Fluids **28**, 1583 (1985).
[16] S. K. Sarkar, Phys. Rev. Lett. **65**, 2680 (1990).

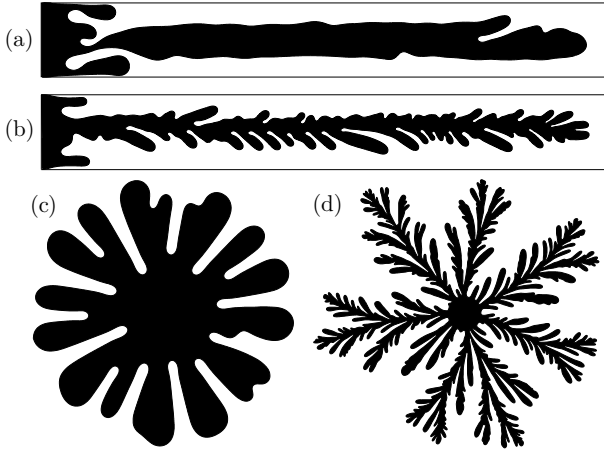


FIG. 1: Viscous fingering patterns of air (black) penetrating into oil (white) in rectangular and circular Hele-Shaw cells for different forcing levels. A fjord is the region of oil between two adjacent fingers. Rectangular cell, (a) $\text{Ca} = 0.0056$ and (b) $\text{Ca} = 0.046$; the rectangles are 25 cm wide and 190 cm long, while the entire cell is 254 cm long. Circular cell, (c) $\text{Ca} = 0.00088$, (d) $\text{Ca} = 0.27$; the radial patterns are approximately 20 cm in diameter, grown in a cell of diameter 28.8 cm. The Ca values were computed using the average velocity of the furthest tip.

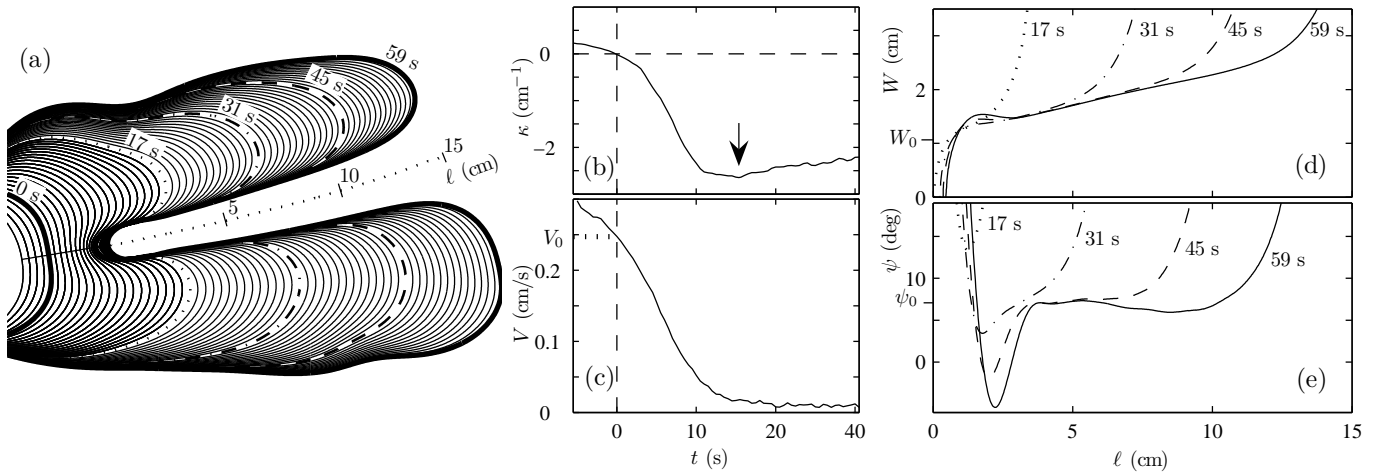


FIG. 2: (a) Time development of a fjord grown in the rectangular cell at $\text{Ca} = 0.0076$ (cf. Fig. 1 caption). Adjacent interfaces are separated by 1 s. (b) Curvature κ and (c) velocity V of a finger tip ($\kappa > 0$) as it evolves into a fjord ($\kappa < 0$) and stops moving; $t = 0$ is the time at which $\kappa = 0$. The velocity V_0 used in computing the instability wavelength, λ_c [Eq. (2)], corresponds to $\kappa = 0$ (here $V_0 = 0.247$ cm/s). The arrow points to the minimum of curvature in time, which defines fjord centerline arc length $\ell = 0$. (d) Fjord width W as a function of the fjord centerline arc length ℓ . The selected fjord base width is given by $W_0 \equiv W(\ell = 0)$; here $W_0 = 1.08$ cm. (e) The opening angle $\psi(\ell)$ between the fjord walls. Here the selected opening angle is $\psi_0 = 7.1^\circ$.

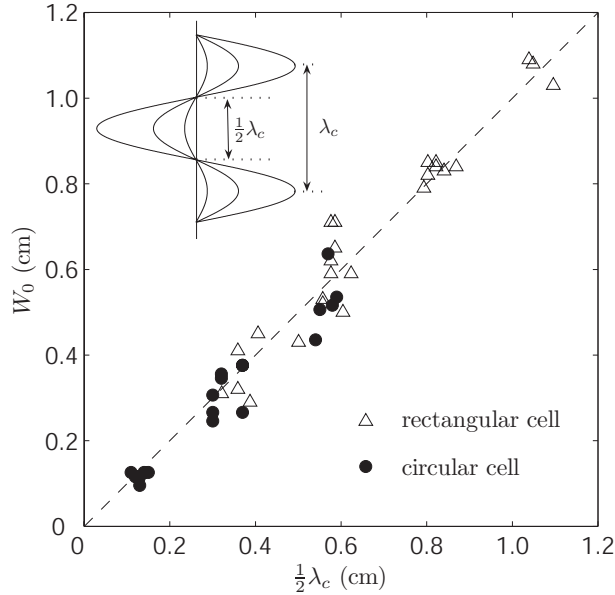


FIG. 3: The measured fjord base width W_0 [cf. Fig. 2(d)] versus the predicted width, $\frac{1}{2}\lambda_c$, where λ_c is the instability wavelength, Eq. (2). The inset illustrates how an initial infinitesimal perturbation of a front (moving to the right) sets the wavelength for a large amplitude fjord.

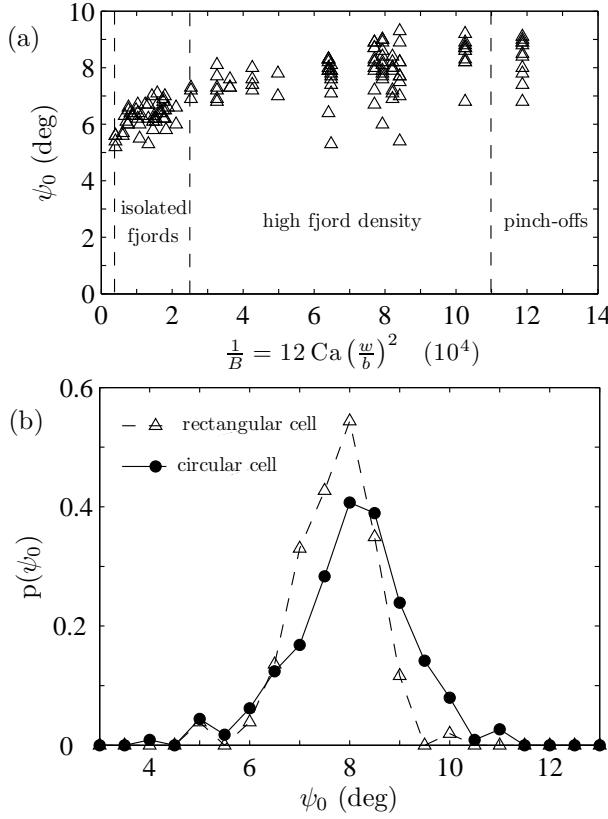


FIG. 4: (a) The fjord opening angle ψ_0 in the rectangular cell initially increases slightly with forcing parameter (the modified capillary number, $\frac{1}{B}$), but in the high fjord density regime ($\frac{1}{B} > 25000$), ψ_0 is constant within the uncertainty of the measurements. (b) Probability distributions measured for the opening angle of all fjords observed in the circular cell (\bullet) and of fjords in the high fjord density regime of the rectangular cell (\triangle). The data for the rectangular and circular cells yield, respectively, $\psi_0 = 7.9 \pm 0.8^\circ$ and $\psi_0 = 8.2 \pm 1.1^\circ$.